Research Article | Vol. 27, No. 4 | 18 Feb 2019 | OPTICS EXPRESS 5048
Optics EXPRESS

Theory and design of Schwarzschild scan objective for Optical Coherence Tomography

GONGPU LAN[1,2] AND MICHAEL D. TWA[2,*]

[1]Foshan University, Department of Photoelectric Technology, Foshan, Guangdong 528000, China
[2]University of Alabama at Birmingham, School of Optometry, Birmingham, Alabama 35294, USA
[*]mtwa@uab.edu

Abstract: Optical coherence elastography (OCE) is one form of multi-channel imaging that combines high-resolution optical coherence tomography (OCT) imaging with mechanical tissue stimulation. This combination of structural and functional imaging can require additional space to integrate imaging capabilities with additional functional elements (e.g., optical, mechanical, or acoustic modulators) either at or near the imaging axis. We address this challenge by designing a novel scan lens based on a modified Schwarzchild objective lens, comprised of a pair of concentric mirrors with potential space to incorporate additional functional elements and minimal compromise to the available scan field. This scan objective design allows perpendicular tissue-excitation and response recording. The optimized scan lens design results in a working distance that is extended to ~140 mm (nearly 2x the focal length), an expanded central space suitable for additional functional elements (>15 mm in diameter) and diffraction-limited lateral resolution (19.33 μm) across a full annular scan field ~ ± 7.5 mm to ± 12.7 mm.

1. Introduction

A Multi-channel optical system contains several independent working channels with various functionalities, such as illumination, mechanical stimulation, imaging, etc. In biomedical and clinical studies, the independent imaging channels could include modalities, such as confocal microscopy, ultrasound, x-ray, magnetic resonance imaging, fluorescence intensity imaging, two-photon imaging, and optical coherence tomography. Compared to a specific single-channel imaging system, multi-channel optical systems can provide complementary, synergistic information, or enable rapid switching between different modes and functions [1]. The use of a multi-channel optical system is helpful to expand the potential uses of non-invasive imaging. For example, dynamic elasticity imaging systems are used to determine tissue mechanical properties (e.g., stiffness) [2,3] by combining a mechanical loading channel (a source of sample stimulation) and an imaging channel to record the sample response.

Optical coherence elastography (OCE) [4] is an emerging elasticity imaging technique that employs at least two channels. A loading channel is used to induce elastic waves in a tissue using techniques, such as optical, mechanical, or acoustic modulators for sample stimulation. Various approaches of loading methods have been developed, such as static [5,6], dynamic contact [4,7–9], audio sound [10], pulsed laser [11,12], and air puff/pulse [13–15] loading. The second channel uses optical coherence tomography (OCT) [16] imaging to record the tissue response. Compared to traditional ultrasound elastography [17–19] and magnetic resonance elastography [20,21], OCT can noninvasively obtain tissue mechanical properties with higher spatial resolution and faster speeds [22]. Phase-sensitive OCT methods [23–27] have further improved the dynamic surface displacement detection sensitivity to a sub-nanometer scale. For example, we reported a 0.24 nm resolution in our common-path OCE results [28]. More channels may be added into the OCE system for specific purposes. For example, a targeting channel and a monitoring camera can be used for locating the regions of stimulus and imaging in the tissue.

#352616 https://doi.org/10.1364/OE.27.005048
Journal © 2019 Received 23 Nov 2018; revised 24 Jan 2019; accepted 26 Jan 2019; published 11 Feb 2019

Optics EXPRESS

The combination of a loading mechanism and OCT imaging usually requires space between the OCT scan objective and sample, especially for dynamic/transient, non-contact OCE applications [10–15]. An optimal OCE set-up should satisfy certain criteria. First, the loading channel should be set up to deform tissue in a predictable way so that tissue mechanical properties can be derived from the deformation response. Loading normal to the surface is advantageous since it simplifies the complex modeling methods that are used to derive the mechanical properties from the observed response [4–6]. Second, measurement distance to the stimulation point should be optimized to clearly record the induced wave-propagation and to avoid near-field effects [29]. Capability of measuring around the stimulation point would also be advantageous to determine tissue anisotropy.

However, spatial conflict often occurs between the physical bulk of the loading system and a limited space provided by the OCT system. Consequently, oblique tissue-excitation has been adopted by several investigators instead of the preferred perpendicular tissue-excitation [7,8,11–14]. The axial distance between the OCT scan objective and sample is usually similar to, or shorter than, the focal length of the scan objective lens. The focal length is often relatively short to achieve a desired optical lateral resolution. For instance, the focal length of the OCT scan lens of our OCE system in [28] was 54 mm, and the total working distance was 42 mm. Therefore, designing a scan objective with a longer working distance without sacrificing optical performance is important for OCE imaging to quantify tissue biomechanics.

Here we describe a novel OCE scan objective comprised of a pair of concentric convex and concave mirrors. This reflective objective is a modification of a Schwarzschild lens design [30]. First-order theory is used to determine the general geometric parameters, especially the focal length, working distance, and dimensional constraint criteria of the Schwarzschild scan objective. Astigmatism for the marginal rays of each scan beam is derived and minimized based on the Coddington equations [31,32]. Optical path differences (OPDs) among all scan beams are reduced to provide effective OCT interference signals from reference and sample arms. The Schwarzschild scan objective extends the working distance and enables adequate free space to accommodate a loading system that can deliver force normal to the tissue surface. Since all the optical elements are mirrors, this Schwarzschild scan objective is free of chromatic aberration and is idea for applications in systems with broad bandwidth (e.g. from visible to near-infrared range that is usually applied in OCT systems).

A Schwarzschild scan objective is designed for, but not limited to, OCE imaging systems. It may also benefit other multi-channel imaging systems that combine peripheral scans with central channels of various purposes. For example, a camera situated in the center area, enclosed by the peripheral scan beams, can serve as a view-finder to guide the scan beams to specific locations. An illumination light source situated in the center of the scan beams may also benefit fluorescence or two-photon imaging.

2. Theory

2.1 Schwarzschild scan objective

The Schwarzschild system [30] was initially designed for astronomical telescopes and was more recently adopted for use in microscope objectives [33–36].The Schwarzschild system consists of two mirrors, as demonstrated in Fig. 1. Previous publications have discussed the use of the Schwarzschild design to correct Seidel aberrations, such as spherical aberration, coma, astigmatism and distortion, and to provide a flat field when the object is either in an infinite or finite distance [33–36].

Optics EXPRESS

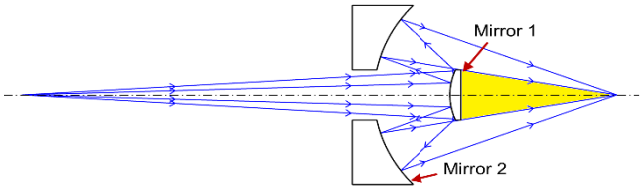

Fig. 1. Schematic of a classic Schwarzschild objective that consists of two mirrors. The object distance is demonstrated in a finite distance. The potential space (yellow shaded region) can be used to include additional channels (e.g. functional elements) to create a multi-channel imaging system.

We extend the application of the Schwarzschild construction to a scan objective that will accommodate additional functional elements for multi-channel imaging (Fig. 1). As demonstrated in Fig. 2, the newly-designed Schwarzschild scan objective is based on the classic Schwarzschild system, but requires modifications to address concerns specifically related to scanning optics. *Mirror 1* is a convex mirror and *Mirror 2* is a concave annular mirror, these two mirrors share the same central point located at the optical axis. Two-dimensional scanners (x and y) are positioned before the scan objective. For simplifying the theory and calculations, we employ one scanner for this analysis. The collimated light beam is demonstrated by a chief-ray and two marginal rays. This beam is scanned by the scanners, is reflected by *Mirror 1* and *Mirror 2* in sequence, then bypasses *Mirror 1* again, and finally is focused at the focal plane.

Figure 2 (a) demonstrates the ray-tracing of the chief ray for a scan beam with the scan angle of θ in the Schwarzschild scan objective. O is the mutual center point of the curvatures of the mirrors. S is the pivot point of the scanner. The chief ray is incident upon the two mirrors at points A and B with angles I_1 and I_2, respectively. C is the exit pupil position. f is the focal length of the Schwarzschild scan objective, and is equal to the distance from point O to the focal plane. L is the total length; d_{work} and d_{exp} are the working distance and exit pupil distance, respectively. Figure 2 (b) demonstrates the ray-tracing of the scan beams with the minimal and the maximal scan angles (θ_{min} and θ_{max}, respectively). The central aperture at the focal plane is $\pm H_{min}$, which precludes imaging within this central area and enables the space for the loading mechanism required by OCE applications. The peripheral annular area at the focal plane — $\pm$ (H_{min} *to* H_{max}), defined by the scan angel range (θ_{min} to θ_{max}) — is available for OCT imaging.

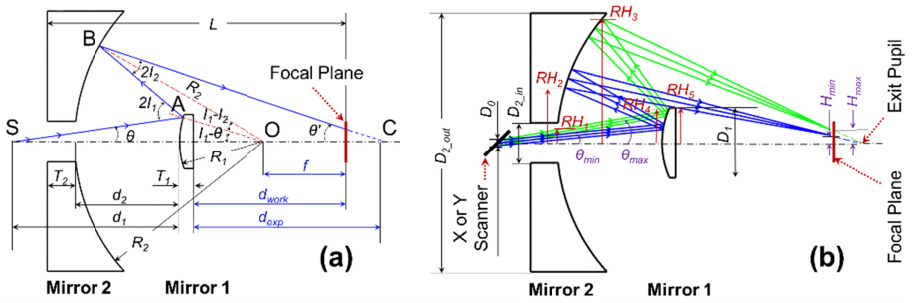

Fig. 2. Configuration geometry of the Schwarzschild scan objective which consists of concentric *Mirror 1* and *Mirror 2*. Only one scanner was shown here for simplicity. (a) Ray-tracing for an arbitrary chief ray with the scan angle of θ. R_1 and R_2 are the radii of curvature, and T_1 and T_2 are the center thickness for *Mirror 1* and *Mirror 2*, respectively. O is the mutual center point of the curvatures of the mirrors. S is the pivot point of the scanner. The distance between point S and *Mirror 1* is d_1, the distance between *Mirror 2* and *Mirror 1* is d_2. The chief ray interacts with the two mirrors at points A and B with incident angles I_1 and I_2, respectively. The chief ray is incident on the focal plane (θ') before the point C (exit pupil position). f is the focal length of the Schwarzschild scan object, and equals to the distance from

Optics EXPRESS

point O to the focal plane. L is the total length. d_{work} and d_{exp} are the working distance and exit pupil distance, respectively. (b) Ray-tracing of the scan beams with the minimal and the maximal scan angles (θ_{min} and θ_{max}, respectively). The reserved central area of loading is in a central zone of $\pm H_{min}$, while the peripheral area of scanning is in the annular zone of $\pm (H_{min} - H_{max})$ at the focal plane. D_0 is the input beam size, D_1 is the diameter of Mirror 1, and D_{2_out} and D_{2_in} are the outer and inner diameters of Mirror 2, respectively. RH_1 to RH_5 are the specific marginal ray heights.

There are some additional concerns in the design of the Schwarzschild scan objective compared to the classic Schwarzschild construction.

(1) The scan angles (θ_{min} to θ_{max}) and the scan zone at the focal plane ($\pm H_{min}$ to $\pm H_{max}$) are constrained by the physical size and distance of the two mirrors. For example, the size of *Mirror 1* should be big enough to reflect the beam with the maximum scan angle (θ_{max}) and should be also small enough to ensure the passage of the beam with the minimum scan angle (θ_{min}) in a non-vignetting condition. Therefore, the modified design incorporated these additional dimensional constraints and established a new criterion to meet the spatial requirements for the Schwarzschild scan objective design.

(2) The light path of the chief ray for each scan beam in the newly-designed Schwarzschild scan objective (Fig. 2(a)) is similar to the light path of each ray in the classic paraxial Schwarzschild construction (Fig. 1). We used methods described in previous work [33–36] to correct Seidel aberrations of the chief rays. However, the layout for each scan beam (Fig. 2(b)) is off-axis with incident angles which can be tens of degrees to the normal of each mirror. Also, the incident angles for all of the scan beams are also over a wide range (tens of degrees). In this application, astigmatism becomes the major contribution to the total aberrations [37] of each scan beam, and the value of astigmatism varies by scan location. Therefore, minimization of astigmatism across the entire scan range was a major design goal.

(3) This Schwarzschild scan objective was developed for an OCT-based elastography application. OCT imaging is a form of low-coherence interferometry where the interference signal is generated by combining light from reference and sample arms [38]. Effective interference requires minimal optical path difference between these two arms. Therefore, the light path length difference among the chief-rays of all the scan beams was constrained to meet the requirement of OCT detection.

2.2 Key points for the Schwarzschild scan objective design

The design principles for the Schwarzschild scan objective are provided as follows:

(1) First-order optical design principles were used to determine the general geometry of the Schwarzschild scan objective that would maximize the axial working distance (defined by the radii of the mirrors (Fig. 2)) without greatly enlarging the radial dimensions of the scan lens for a specified scan range. The extended working distance was derived by calculating the axial dimensions and the radial dimensions were primarily determined by the defined scan range.

(2) The Coddington equations [31,32] were applied to quantify the astigmatism, defined as the difference in focal distance between the tangential and sagittal marginal rays [39,40] for each scan beam. The astigmatism value across the whole scan range was then evaluated and minimized by optimizing the design parameters.

(3) The chief-ray optical length (OPL) was calculated for each scan beam. The optical path differences (OPDs) of all the chief-rays from all of the scan beams were estimated. The OPD values were balanced with other design requirements (e.g. size

Optics EXPRESS

of the system, astigmatism) to enable the use of the Schwarzschild scan objective in OCT imaging.

The detailed theoretical analysis for the above design concerns are discussed in the following sections.

2.3 Axial dimensions and working distance extension

The radii of curvatures for *Mirror 1* and *Mirror 2* are R_1 and R_2, respectively, both are defined as positive values. The focal lengths of these two mirrors are $f_1 = -R_1 / 2$ and $f_2 = R_2 / 2$. We define $R_2 = M \times R_1$ ($M > 1$), where M is ratio of the raddi of curvatures as well as the ratio of focal lengths between two mirrors. The distance between scanner and *Mirror 1* is d_1. The distance between *Mirror 2* and *Mirror 1* is d_2, where $d_2 = R_2 - R_1$ because *Mirror 1* and *Mirror 2* are concentric. The total focal length f of the objective can be calculated as:

$$f = \frac{f_1 f_2}{f + f_2 - d_2} = \frac{MR_1}{2(M-1)}, \tag{1}$$

where $M = 2f / (2f - R_1)$, $R_2 = 2fR_1 / (2f - R_1)$, and $d_2 = R_1^2 / (2f - R_1)$.

The exit pupil distance d_{exp} is defined as the axial distance from *Mirror 1* to the exit pupil, and the working distance d_{work} is defined as the axial distance from *Mirror 1* to the focal plane. d_{exp} and d_{work} can be expressed as:

$$d_{\exp} = \left[\frac{Md_1 + MR_1}{2d_1(M-1) + R_1(M-2)} + 1 \right] \times R_1 - T_1, \tag{2}$$

$$d_{work} = \left(\frac{M}{2M-2} + 1 \right) \times R_1 - T_1, \tag{3}$$

where T_1 and T_2 are the center thicknesses for the two mirrors. Comparing Eq. (1) and Eq. (3), we have:

$$d_{work} = f + R_1 - T_1, \tag{4}$$

If $R_1 > T_1$, then $d_{work} > f$. Therefore, the working distance can be extended to a longer value than the focal length. For the same value of f, d_{work} is increased by the same amount as R_1 is increased. Therefore, f is equal to the distance from the mutual center point of the two mirrors to the focal plane. The total length L from *Mirror 2* to the focal plane can be expressed as:

$$L = T_1 + R_2 + f = \frac{(2M-1)}{2(M-1)} \times MR_1 + T_1. \tag{5}$$

2.4 Radial dimensions and dimensional constraint criteria

Scan angle θ is in the range of θ_{min} to θ_{max}, its corresponding scan length H ($H = f \tan\theta$) at the focal plane is in the range of H_{min} to H_{max}. Figure 2 depicts RH_1 to RH_5, the specific marginal ray heights. RH_1 is the maximum ray height inside the center hole of Mirror 2. RH_2 and RH_3 are the inner and outer ray heights for the light annulus on *Mirror 2*. RH_4 is the maximum ray height at the front surface of *Mirror 1*, and RH_5 is the minimum ray height at the back surface of *Mirror 1*. These marginal ray heights can be expressed as:

Optics EXPRESS

$$\begin{cases} RH_1 = (d_1 - d_2)\tan\theta_{\max} + \dfrac{D_0}{2}, \\ RH_2 = \left[d_1(2M-1) + R_1(M-1)\right] \times \tan\theta_{\min} - \dfrac{(2M-1)}{2} D_0, \\ RH_3 = \left[d_1(2M-1) + R_1(M-1)\right] \times \tan\theta_{\max} + \dfrac{(2M-1)}{2} D_0, \\ RH_4 = d_1 \tan\theta_{\max} + \dfrac{D_0}{2}, \\ RH_5 = \left\{1 - \dfrac{\left[2d_1(M-1) + R_1(M-2)\right]\left[R_1(M-1) + T_1\right]}{MR_1\left[d_1(2M-1) + R_1(M-1)\right]}\right\} \\ \quad \times \left\{\left[d_1(2M-1) + R_1(M-1)\right]\tan\theta_{\min} - \dfrac{(2M-1)}{2} D_0\right\}, \end{cases} \tag{6}$$

where D_0 is the entrance pupil size or beam size, D_1 is the diameter of Mirror 1, and D_{2_out} and D_{2_in} are the outer and inner diameters for Mirror 2. The expressions for RH_1 to RH_5 all consist of two components. The first component contains either $\tan\theta_{max}$ or $\tan\theta_{min}$, and denotes the chief ray heights. The second component contains D_0, and denotes the half beam size at the corresponding surface.

To avoid vignetting in *Mirror 1* and *Mirror 2*, the following dimensional criteria should be satisfied:

$$\begin{cases} \dfrac{2RH_3}{\rho_{2\_out}} \le D_{2\_out}, \\ 2RH_1 \le D_{2\_in} \le 2RH_2 \times \rho_{2\_in}, \\ \dfrac{2RH_4}{\rho_1} \le D_1 \le 2RH_5, \end{cases} \tag{7}$$

where ρ_1, ρ_2, and ρ_{2_out} are the ratios for the clear aperture (usually, $\rho \approx 90\%$). The first criterion defines the minimum requirement for D_{2_out}. The second criterion ensures the vignetting-free condition for *Mirror 2* where the scan beams can go through the center hole, and the reflected beams from *Mirror 1* can reach the effective optical portion of *Mirror 2*. The third criterion determines the vignetting-free condition for *Mirror 1* so that the scan beams can be reflected by the clear aperture of *Mirror 1*, while the reflected light from *Mirror 2* can bypass the outside diameter of *Mirror 1*.

2.5 Optical path length (OPL) and optical path difference (OPD)

To guarantee the effective interference between the signals from the sample arm (where OPL varies across the field of view) and the reference arm (where OPL is a constant value), the OPD from all the chief-rays across the scan field in the sample arm must be limited to a certain range. As shown in Fig. 2, The OPL for this chief ray is dominated by R_1 and θ and can be expressed as:

Optics EXPRESS

$$\begin{aligned} OPL(R_1,\theta) &= \left|\overrightarrow{SA}\right| + \left|\overrightarrow{AB}\right| + \left|\overrightarrow{BC}\right| \\ &= \frac{\sin(I_1-\theta)(\sin\theta+\sin I_2)}{\sin\theta\sin I_2}\times R_1 + \frac{1+2(M-1)\cos(2I_1-I_2-\theta)}{2(M-1)\cos(2I_1-2I_2-\theta)}\times MR_1, \end{aligned} \tag{8}$$

where

$$\begin{cases} I_1 = \arcsin\left(\dfrac{d_1+R_1}{R_1}\times\sin\theta\right), \\ I_2 = \arcsin\left(\dfrac{d_1+R_1}{R_2}\times\sin\theta\right). \end{cases} \tag{9}$$

The maximum OPD from all the chief-rays across the scan field can be expressed as:

$$OPD_{\max}(R_1,\theta) = OPL(R_1,\theta_{\max}) - OPL(R_1,\theta_{\min}). \tag{10}$$

2.6 Astigmatism

As shown in Fig. 2, the layout for each scan beam is off-axis with large incident angles relative to the surface normal for each mirror. In this mirror-based, off-axis construction, the dominant aberration is astigmatism [37], defined as the difference in focal distance between the tangential and sagittal marginal rays [39,40]. Applying the Coddington equations [31,32] to *Mirror 1* and *Mirror 2*, we can express the general astigmatism (AST) as:

$$AST(R_1,0) = \frac{MR_1(2M-2+\cos I_1)\cos I_2}{4(M-1)+2\cos I_1-2M\cos I_2} - \frac{MR_1[(2M-1)+\sec I_1]}{2\cos I_2[2(M-1)+\sec I_1-2M} \tag{11}$$

Corresponding to the different scan angle θ, the value of astigmatism varies across the scan field. We define a discrete mean absolute astigmatism (DMAA) equation to minimize the total amount of astigmatism in the required scan range:

$$DMAA = \frac{\sum_{i=0}^{k} a_i \left|AST(R_1,\theta_i)\right|}{\sum_{i=0}^{k} a_i}, \tag{12}$$

where $\theta_i = \theta_{min} + i(\theta_{max} - \theta_{min})/k$, k is the step number ($i = 0, \ldots, k$), and α_i is the weight.

3. Quantitative simulation

We performed a quantitative simulation to demonstrate the design of the Schwarzschild scan objective. We first specified the design requirements and then computed the possible R_1 values that met each of the design requirements separately. We then optimized R_1 to simultaneously satisfy all of the requirements.

3.1 Design requirements

The design parameters for this Schwarzschild scan objective were defined by the current specifications of our clinical OCE system [28]. The spectral bandwidth of the OCT light source was 795 nm – 895 nm, D_0 = 4 mm, and f = 75 mm, the lateral resolution was 19.33 μm, calculated at the central wavelength of 845 nm. The requirements for the loading and scanning space were specified as $d_{work} \geq 120$ mm, $2H_{min} \geq 10$ mm, and H_{max} to $H_{min} \approx 5$ mm. The dimensional requirements were specified as $D_1 \leq 70$ mm, $D_{2\_out} \leq 200$ mm, $T_1 = 10$ mm, $T_2 = 20$ mm – 30 mm, and $L \leq 300$ mm. The distance requirements for the X and Y scanners

Optics EXPRESS

were set to d_{1Y} - d_{1X} = 12.7 mm, and $d_{1X} \geq d_2 + T_2 + 15$ mm. To simplify the calculation and keep the structure compact, we assigned $d_1 = (d_{1X} + d_{1Y})/2 = d_2 + 51.35$ mm. This scan objective was designed for an OCT system with the capability of detecting 6.5 mm OPD between the sample arm and the reference arm. We specified the maximum OPD range across the entire FOV in the sample arm as 1.5 mm.

3.2 Computing R_1 values to meet each requirement

The key variable in the calculation and optimization is R_1, which is in the range of 0 to 2f. Here, we reduced its range to 0.5f to 1.5f (37.5 mm to 112.5 mm) to avoid extreme values in dimensions and aberrations.

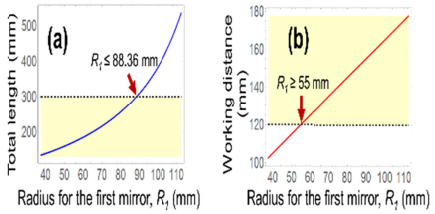

Fig. 3. Axial dimensions of (a) total length L and (b) working distance d_{work}. To meet the requirements of $L \leq 300$ mm and $d_{work} \geq 120$ mm, R_1 should be in the range of 55 mm – 88.36 mm (yellow-shaded areas).

Figure 3 shows the axial dimensions for L and d_{work} corresponding to R_1, when f = 75 mm. To satisfy the requirements of $L \leq 300$ mm and $d_{work} \geq 120$ mm, R_1 should be in the range of 55 mm to 88.36 mm. As R_1 increased, d_{work} increased by the same amount, provided T_1 was kept constant (Eq. (4)).

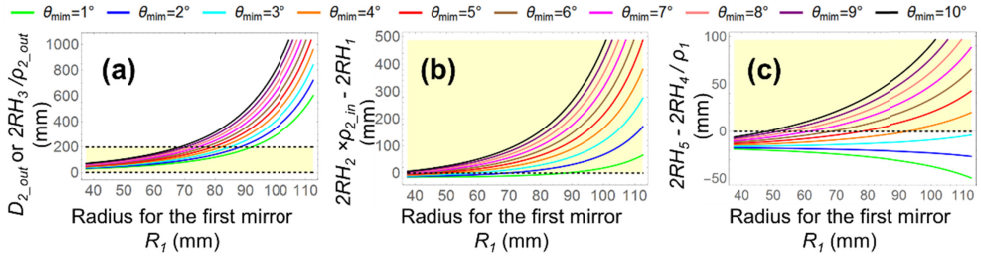

Fig. 4. Marginal ray tracing for RH_1 to RH_5, to satisfy the dimensional constraint criteria in Eq. (7) for different values of R_1 and θ_{min}. (a) Satisfaction of first criterion, representing the minimum diameter for D_{2_out}. (b) Satisfaction of second criterion, representing the vignetting-free condition around the center hole in *Mirror 2*. (c) Satisfaction of the third criterion, representing the vignetting-free condition for *Mirror 1* ($\rho_1 = \rho_{2\_out} = \rho_{2\_in}$ = 90%). Yellow-shaded areas show the radial dimensional constraint requirements.

The marginal rays for RH_1 to RH_5 were traced to satisfy the dimensional criteria in Eq. (7). Figure 4 (a) corresponds to the first constraint, which defines the minimum value for D_{2_out} (ρ_{2_out} = 90%). The required D_{2_out} increased when R_1 was increased. A larger D_{2_out} would be more difficult to manufacture and result in higher manufacturing costs. Thus, limiting D_{2_out} to as small a value as possible, such as in a range smaller than 200 mm, was found to be beneficial, while still satisfying the design requirements.

Figures 4 (b) and (c) represent the second and third criteria that enable the vignetting-free conditions for *Mirror 1* and the center hole region of *Mirror 2*, where $\rho_1 = \rho_{2\_in}$ = 90%. These two criteria are met once the marginal height differences in both criteria are no less than zero, shown as yellow-shaded areas. As shown in Fig. 4 (b), once R_1 was set to a larger value, the second criteria was met with a smaller minimum scan angle θ_{min}. Figure 4 (c) shows that when θ_{min} = 1° to 3°, $2RH_5$ - $2RH_4$ / ρ_1 <0, and the light beams would not bypass *Mirror 1*,

Optics EXPRESS

irrespective of the value of R_1 value. When $\theta_{min} \geq 4°$, as R_1 was increased, the minimum required θ_{min} was decreased. For each θ_{min}, the desired R_1 range to meet the third criterion was found to be within the R_1 range required to meet the second criterion. Thus, the third criterion in this design was stricter than the second criterion. That is, satisfying the third criterion assured the satisfaction of the second criterion.

D_{2_in} was set to a value between $2RH_1$ and $2RH_2 \times \rho_{2\_in}$. Therefore, we utilized the minimum requirement of the third criterion ($2RH_4/\rho_1 = 2RH_5$) to calculate the desired scan angle range (θ_{min} to θ_{max}) and scan length range (H_{min} to H_{max}), as a function of R_1 (Fig. 3 (a) and (b)). When R_1 was increased, the minimum required θ_{min} was decreased. This result was consistent with Fig. 4 (c). Thus, both the scan angles and scan lengths were reduced.

Once the scan angle range (θ_{min} to θ_{max}) was determined, we computed the diameter requirements for D_1 and D_{2_out} as a function of R_1 (Fig. 5 (c)). To meet the requirement of $D_1 \leq 70$ mm and $D_{2\_out} \leq 200$ mm, R_1 was required to be less than 79.60 mm.

Figure 5 (d) shows the OPD_{max} curve we computed by substituting θ_{min} and θ_{max} from Fig. 5 (a) into Eqs. (8), (9), and (10). When $R_1 = 41.67$ mm then $OPD_{max} = 0$, when $R_1 < 41.67$ mm then $OPD_{max} > 0$, and when $R_1 > 41.67$ mm then $OPD_{max} < 0$. To restrict OPD in the range of ± 1.5 mm, R_1 was required to be in the range of 37.5 mm to 93.80 mm.

Based on Eqs. (9) and (11), the changes in astigmatism caused by R_1 and θ are shown in Fig. 5 (e). Larger values for θ were associated with a steeper slope for the relationship between astigmatism and R_1. Thus, for astigmatism reduction, the possible R_1 values were in a wider range when θ was a relatively small value, and the possible R_1 were in a narrower range when θ had a larger value. Given a certain value of θ, a corresponding R_1 can be selected to minimize astigmatism. However, given a range of θ, astigmatism cannot be fully eliminated. Thus, we computed the discrete mean absolute astigmatism (*DMAA*) (Eq. (12)) for the scan angle range of θ_{min} to θ_{max}, where $\alpha_i = 1$, and $k = (\theta_{max}$ to $\theta_{min})/0.01°$. As shown in Fig. 5 (f), for the minimum value of $DMAA = 0.2033$ mm, R_1 equaled 86.26 mm.

If different weights (α_i) were assigned, e.g. more weight for the center field and less weight for the edge field, or *vice versa*, the optimal R_1 value calculated by the *DMAA* method was between 80 mm and 90 mm.

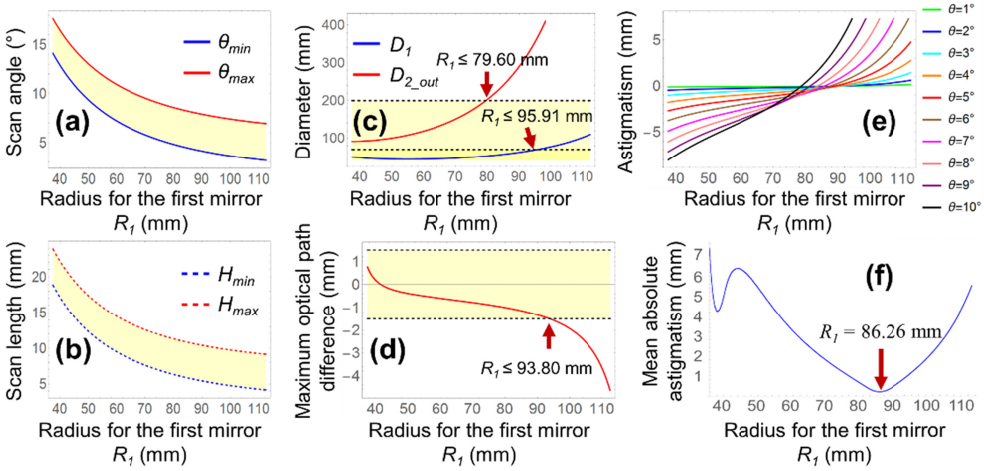

Fig. 5. The equality $2RH_4/\rho_1 = 2RH_5$ was used to determine (a) θ_{min} to θ_{max}, (b) H_{min} to H_{max}, (c) D_1 and D_{2_out}, and (d) OPD_{max} in related to the radius of the *Mirror 1* (R_1). Yellow-shaded areas in (a) to (d) represent the desired value ranges. (e) Astigmatism for general scan angles (1° to 10°, with a step of 1°) without considering the physical constraints. (f) Astigmatism minimization using *DMAA* method (when $\alpha_i = 1$) for the constraint-determined scan angle range of θ_{min} to θ_{max}.

Optics EXPRESS

3.3 Calculation summary and optimization of R_1

The requirements for the key design parameter R_1 were:

(1) To achieve the dimensional requirements of $L \leq 300$ mm and $d_{work} \geq 120$ mm, R_1 was limited to the range of 55 mm to 88.36 mm.

(2) To relate all of the scan-related parameters (θ_{min} to θ_{max}, H_{min} to H_{max}, D_1, D_{2_out}, OPD, and astigmatism) to R_1, the minimum requirement of the third criterion in Eq. (8) was used, where $2RH_4/\rho_1 = 2RH_5$.

(3) To meet the diameter requirements of $D_1 \leq 70$ mm and $D_{2\_out} \leq 200$ mm, R_1 was required to be less than 79.60 mm.

(4) To restrict the absolute value of OPD_{max} less than 1.5 mm, R_1 was required to be in the range of 37.5mm to 93.80 mm. When $R_1 = 41.67$ mm, then $OPD_{max} = 0$; when 37.5 mm $\leq R_1 <$ 41.67 mm, then $0 < OPD_{max} \leq 0.76$ mm; and when 41.67 mm $< R_1 \leq$ 93.80 mm, then -1.5 mm $\leq OPD_{max} < 0$.

(5) To reduce the astigmatism for the entire scan field, R_1 was required to be in the range of 80 mm to 90 mm.

To satisfy requirements (1) to (5), R_1 was found to be optimal in the range 55 mm to 79.60 mm, where the requirements for L, d_{work}, D_{2_out} and OPD_{max} were met. However, this range of values for R_1 did not minimize astigmatism. Since the residual astigmatism decreased as the value of R_1 was increased in the range 55 mm – 79.60 mm (Fig. 5 (f)), we chose a relatively large R_1 value (75 mm). Note that, aspherical surfaces can be used to further minimize residual astigmatism and other aberrations.

4. Zemax validation and design results

We employed the optical design software Zemax (Zemax, LLC) to validate the calculation, and to finalize the design. *Mirror 1* was designed as an aspherical mirror to further reduce aberrations. A low-order standard aspherical surface is given by [41]:

$$z(r) = \frac{r^2 / R_1}{1 + \sqrt{1 - (1 + k_1) r^2 / R_1^2}}, \tag{13}$$

where the optical axis is presumed in the z direction, $z(r)$ is the sag value (the displacement of surface in the z direction from the vertex at a distance of r from the optical axis), and r is in the range 0 to $0.5\rho_1 D_1$. The conic constant k_1 of the aspherical *Mirror 1* was set as the only variable to be optimized, along with all of the other parameters that were calculated in Section 3. The aspherical surface type is determined by k_1, and can be hyperbola ($k_1 < -1$), parabola ($k_1 = -1$), prolate ellipse ($-1 < k_1 < 0$), sphere ($k_1 = 0$), or oblate ellipse ($k_1 > 0$).

Optics EXPRESS

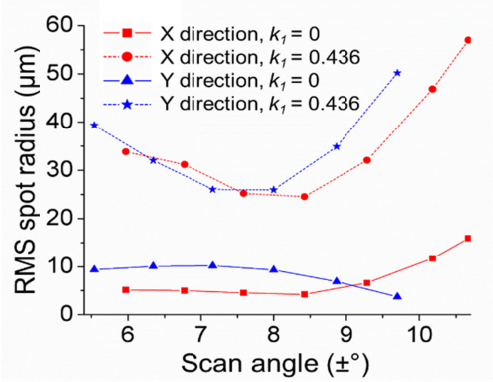

Fig. 6. RMS spot size reduction by employing an aspherical (k_1 = 0.436, solid lines) Mirror 1, compared to when Mirror 1 is spherical (k_1 = 0, dotted lines).

Using the damped least square algorithm in Zemax, k_1 was optimized to 0.436. For the two scanners, d_{1x} and d_{1y} were computed to be 120 mm and 134.7 mm, respectively. The scan fields in the *x*-direction and in *y*-direction were ± (5.97° to 10.67°) and ± (5.54° to 9.70°), respectively. The root mean square (RMS) spot sizes was reduced significantly across the scan field in both *x* and *y* directions when *Mirror 1* was modeled as an oblate ellipsoid (since $k_1 > 0$), as shown in Fig. 6.

All of the optical elements in this Schwarzschild scan objective were mirrors (Fig. 7), ensuring no chromatic aberrations in broad bandwidths. The light coming out of the fiber was collimated by a parabolic reflective collimator (RC04FC-P01, Thorlabs), and then scanned by Galvo mirrors (GVS012, Thorlabs) in the *x* and *y* directions. The scan beams then passed through a 1-inch center hole in Mirror 2, were reflected by the concave Mirror 1 with 75 mm radius, and then reflected by the concave Mirror 2 with 150 mm radius. The outside diameters for Mirror 1 and Mirror 2 were 200 mm and 56 mm, respectively, and the outside clear apertures were 90% of their diameters. The distance between the two mirrors was 75 mm. The thicknesses of Mirror 1 and Mirror 2 were 10 mm and 30 mm, respectively. Mirror 1 was mounted using a three-arm holder vane. The working distance between the back of Mirror 1 to the focal plan was 139.8 mm.

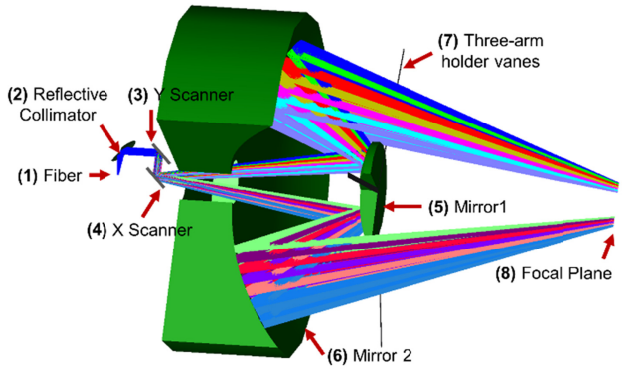

Fig. 7. Schematic of the Schwarzschild scan objective, designed using the outcome of the design requirement analysis and Zemax software simulation (drawed in 3/4 section).

Figure 8 (a) shows a quasi-linear relation between the scan angles and scan lengths in the *x* and *y* directions, simulated in Zemax. This result was used to calibrate the lateral distortion for the objective. Figure 8 (b) shows the OPD across the scan fields, relative to the minimum scan angles, 5.97° in *x* direction and 5.54° in y direction. The maximum OPD across the scan

Optics EXPRESS

field was 1.34 mm. The OPLs at bigger scan angles were found to be shorter. Figure 8 (b) can be used in the digital calibration to offset the axial distortion generated by OPD.

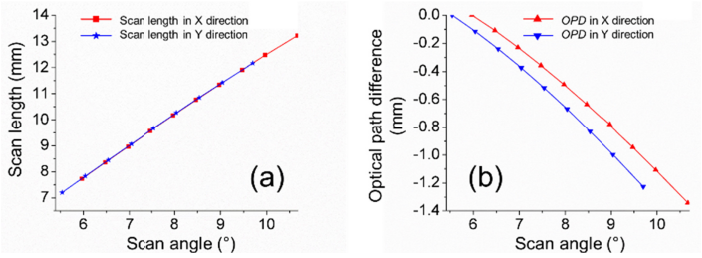

Fig. 8. Distortion calibration in Zemax simulation. (a) Lateral distortion, demonstrated by the relation between scan angle and scan length. (b) Axial distortion, demonstrated by optical path difference (OPD) across the scan field.

Figure 9 shows the tissue-excitation (loading) and the wave-detection (scanning) areas, as well as the spot diagrams of selected wavelengths (795 nm, 845 nm, and 895 nm) at the focal plane, simulated in Zemax. The scanning area was an elliptical annulus zone of ± (7.73 mm to 13.22 mm) in the *x* direction and ± (7.20 mm to 12.17 mm) in the *y* direction, centered at the optical axis. The loading area was an elliptical zone of ± 7.73 mm in the *x* direction and ± 7.20 mm in the *y* direction. The spots at different fields are shown as 1-mm intervals in scan length. These spots were free of chromatic aberration, and were scaled using the Airy disc at 845 nm wavelength, whose radius is theoretically 19.33 μm for a circular, uniformly illuminated entrance pupil. Therefore, the elliptical shapes of some circles are caused by non-uniform illuminations due to oblique light incidences. The radius of the Airy disc is equal to the minimum resolvable detail (diffraction-limited resolution) based on the Rayleigh criterion. If all of the rays are well within the Airy disk, then the system is often said to be diffraction-limited [41]. Except for several out-of-focus spots at the edge of the scan field, all other spots were within the Airy disk circles. The maximum RMS radius for the spots at the edge of the scan FOV was 16.49 μm, still smaller than the Airy disc radius. Thus, this scan objective was diffraction-limited. If each arm of the holder vane for Mirror 1 was 3 mm in width, the obscuration (shadow areas in Fig. 9) due to each arm is ~3 mm at the inner ellipse and ~2 mm at the outer ellipse in the scanning area.

Optics EXPRESS

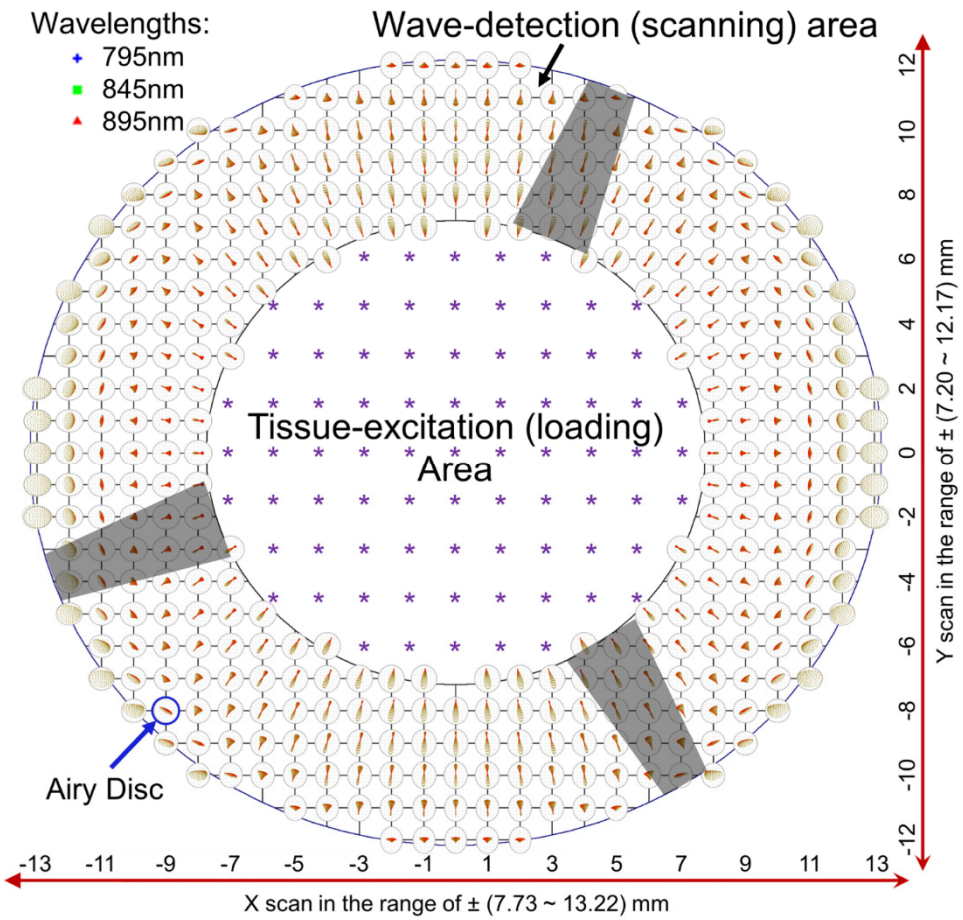

Fig. 9. Demonstration of the tissue-excitation (loading) and the wave-detection (scanning) areas, as well as the spot diagrams at the focal plane, simulated in Zemax. The purple stars show the possible loading locations. The distance between two spots is 1mm in the x and y directions. The shadow areas are due to the obscuration of the Mirror 1 mount.

5. Discussion

5.1 Non-uniform illumination due to angle of incidence

We used a telecentric scan lens in our previous OCE system [28] where the chief rays of scan beams were parallel to the optical axis and perpendicular to the focal plane. Compared to the non-telecentric construction, the telecentric scan lens can illuminate the sample more uniformly and collect more reflected/scattered light back to the system with a flat sample geometry (e.g. 2% agar phantom [28]).

In the Schwarzschild scan objective, scan beams are not perpendicular to the focal plane and the incident angel (θ') varies across different scan positions. In the design example of Section 4, the incident angels at the focal plane vary from 9.88° to 19.14° in the x direction, and from 10.09° to 19.05° in the y direction. Illumination is positively correlated with $cos^4(\theta')$. When the sample surface was flat, the illuminance values were calculated as 94.2% – 79.7% in the x direction, and 94.0% – 79.8% in the y direction, relative to the perpendicular illumination.

Tissue samples may have any shape including convex surface geometry, such as the cornea [42]. In our previous work, we have quantified the biomechanical properties of rabbit [43–45] and porcine [46–49] corneas. We noticed that the imaging intensities and phase

Optics EXPRESS

sensitivities dropped noticeably when imaging away from the apex or in the peripheral regions of the cornea using a telecentric scan lens. In this case, a scan lens with a convergent scan beam geometry would provide greater tissue illumination and back-light collection for better image contrast than a telecentric scan lens. The design example presented in section 4 has a larger work space relief to accommodate a loading channel for corneal OCE applications. Future designs could also include a convergent beam scan lens for other applications.

5.2 Design alternative I: optimizing d_1 to further reduce OPD

In Section 3.3, the required R_1 range was found to be 55 mm to 79.60 mm. Instead of choosing a smaller value (for example 55 mm) to reduce the OPD, we selected a value of 75 mm to reduce astigmatism. This resulted in a maximum absolute OPD of 1.34 mm, across the entire scan field (Fig. 8 (b)).

Without compromising the correction of astigmatism, another possibility for *OPD* reduction would be to adjust the value of d_1. Our calculations and simulations demonstrated that a smaller d_1 reduced OPD. However, the scanning mirrors in our design were big and had to be located to the left side of *Mirror 2* (Fig. 7), resulting in a relatively big d_1 (120 mm and 134.7 mm, respectively for the two scanners). Using smaller scanners and mounts might reduce d_1 and further reduce OPD, if they can be located between *Mirror 1* and *Mirror 2*.

5.3 Design alternative II: using spherical surfaces for both mirrors

For astigmatism minimization, we designed Mirror 1 as a standard aspherical mirror with a small diameter (56 mm) and small departures (k = 0.436) from a standard spherical mirror. The manufacturing cost for such a mirror is inexpensive.

If a larger R_1 value is chosen, such as 90 mm, both mirrors can be spherical surfaces and still achieve diffraction-limited performance. However, a larger R_1 will require a larger diameter Mirror 2 (> 300 mm). This would greatly increase the cost of manufacturing and mirror verification.

5.4 Design alternative III: splitting Mirror 2 as multiple small mirrors

Some specific applications may require better lateral resolution (related to D_0/f) or a need to accommodate larger scan areas (related to scan angles). Consequently, *Mirror 2* with a larger aperture (e.g. > 200 mm) may be required to meet these demands. However, fabrication of a larger aperture of *Mirror 2* is more difficult and expensive. A possible solution is to split *Mirror 2* into multiple small mirrors, e.g. two or four mirrors. This mirror-splitting method can reduce the fabrication cost, but will require more complex construction as well as higher assembly cost.

5.5 Design alternative IV: mounting Mirror 1 onto glass to reduce obscuration

Holder vanes are commonly applied for mounting the small mirror into a two-reflector telescope, such as in the construction of Schwarzschild [30] and Cassegrain [50] lenses. Since the small mirror is usually located at the pupil plane in a conventional telescope, holder vanes do not generate blind spots at the image plane.

In our design, since *Mirror 1* is not located at the pupil plane (Fig. 7), the three-arm holder vanes would induce obscurations at the focal plane (Fig. 9). Use of a flat glass window to mount *Mirror 1* can effectively avoid such obscurations. We have performed the Zemax simulation using a 10-mm thick glass window (material: BK7) to mount *Mirror 1* instead (wavelength: 795–895 nm). The point spread functions in the same scan areas are still diffraction-limited with only slightly increased chromatic dispersions over this wavelength range and this validates this glass window mount as a viable option. In addition, the reflective collimator used in Fig. 7 can be replaced by an achromatic lens-based collimator for this wavelength range as well. Choosing the mounting method would be determined by the

Optics EXPRESS

specific design requirements, such as wave bandwidth, numerical number, scan angles, and complexity, as well as the preference of the designer.

6. Conclusion

We demonstrated the theory and design for an OCE reflective scan objective by employing a Schwarzschild design with two concentric convex and concave mirrors. This Schwarzschild scan objective extended the working distance, and enabled the use of central perpendicular tissue-excitation with peripheral wave-detection.

We presented a detailed theory in Section 2, where R_1 was chosen as the key value to calculate, optimize, and evaluate the main parameters, such as the axial dimensions, radial dimensions, radial constraints and dimensional criteria, OPD among chief rays, and astigmatism values for the scan beams.

In Section 3, the relation between the axial dimensions (L and d_{work}) and R_1 was demonstrated. The equation of $2RH_4/\rho_1 = 2RH_5$ was used to further relate R_1 to other parameters, such as scan angles, scan lengths at the focal plane, OPD among chief rays, and astigmatism for the scan beams. After balancing all of these key design constraints, especially D_{2_out}, we chose $R_1 = 75$ mm.

In Section 4, we defined the conic constant for *Mirror 1* surface as the only variable, and optimized this scan objective to further reduce astigmatism and the residual aberrations (Fig. 6). The reflective configuration provided a chromatic-aberration-free design. This feature enables its use in broad bandwidths (e.g. from visible to near-infrared range that is usually applied in OCT imaging). Lateral distortion (relation between the scan angle and scan length) and axial distortion (OPD) were presented for system calibration (Fig. 8). Regions of loading and scanning were defined and the diffraction-limited performance was achieved (Fig. 9).

In summary, a Schwarzschild scan objective was designed for broad bandwidth optical coherence elastography with a long working distance, central perpendicular tissue-excitation, and peripheral wave-detection. *OPD* of the chief rays and astigmatism values for the scan beams were reduced and the lateral resolution was diffraction-limited for the entire scan field. This Schwarzschild scan objective may also benefit other multi-channel imaging systems that combine peripheral scans with other central channels.

Funding

This study was supported by the following grants: NIH/NEI R01-EY022362, P30EY07551, and P30EY003039 from United States; and the Foshan University start-up fund Gg07071 from China

References

1. J. Y. Hwang, S. Wachsmann-Hogiu, V. K. Ramanujan, J. Ljubimova, Z. Gross, H. B. Gray, L. K. Medina-Kauwe, and D. L. Farkas, "A multimode optical imaging system for preclinical applications in vivo: technology development, multiscale imaging, and chemotherapy assessment," Mol. Imaging Biol. **14**(4), 431–442 (2012).
2. J. F. Greenleaf, M. Fatemi, and M. Insana, "Selected methods for imaging elastic properties of biological tissues," Annu. Rev. Biomed. Eng. **5**(1), 57–78 (2003).
3. A. Sarvazyan, T. J. Hall, M. W. Urban, M. Fatemi, S. R. Aglyamov, and B. S. Garra, "An overview of elastography-an emerging branch of medical imaging," Curr. Med. Imaging Rev. **7**(4), 255–282 (2011).
4. J. Schmitt, "OCT elastography: imaging microscopic deformation and strain of tissue," Opt. Express **3**(6), 199–211 (1998).
5. J. Rogowska, N. A. Patel, J. G. Fujimoto, and M. E. Brezinski, "Optical coherence tomographic elastography technique for measuring deformation and strain of atherosclerotic tissues," Heart **90**(5), 556–562 (2004).
6. R. Chan, A. Chau, W. Karl, S. Nadkarni, A. Khalil, N. Iftimia, M. Shishkov, G. Tearney, M. Kaazempur-Mofrad, and B. Bouma, "OCT-based arterial elastography: robust estimation exploiting tissue biomechanics," Opt. Express **12**(19), 4558–4572 (2004).
7. C. Li, G. Guan, R. Reif, Z. Huang, and R. K. Wang, "Determining elastic properties of skin by measuring surface waves from an impulse mechanical stimulus using phase-sensitive optical coherence tomography," J. R. Soc. Interface **9**(70), 831–841 (2012).

Optics EXPRESS

8. S. Song, Z. Huang, T.-M. Nguyen, E. Y. Wong, B. Arnal, M. O'Donnell, and R. K. Wang, "Shear modulus imaging by direct visualization of propagating shear waves with phase-sensitive optical coherence tomography," J. Biomed. Opt. **18**(12), 121509 (2013).
9. B. F. Kennedy, T. R. Hillman, R. A. McLaughlin, B. C. Quirk, and D. D. Sampson, "In vivo dynamic optical coherence elastography using a ring actuator," Opt. Express **17**(24), 21762–21772 (2009).
10. B. I. Akca, E. W. Chang, S. Kling, A. Ramier, G. Scarcelli, S. Marcos, and S. H. Yun, "Observation of sound-induced corneal vibrational modes by optical coherence tomography," Biomed. Opt. Express **6**(9), 3313–3319 (2015).
11. C. Li, G. Guan, Z. Huang, M. Johnstone, and R. K. Wang, "Noncontact all-optical measurement of corneal elasticity," Opt. Lett. **37**(10), 1625–1627 (2012).
12. C. Li, Z. Huang, and R. K. Wang, "Elastic properties of soft tissue-mimicking phantoms assessed by combined use of laser ultrasonics and low coherence interferometry," Opt. Express **19**(11), 10153–10163 (2011).
13. S. Wang, K. V. Larin, J. Li, S. Vantipalli, R. K. Manapuram, S. Aglyamov, S. Emelianov, and M. D. Twa, "A focused air-pulse system for optical-coherence-tomography-based measurements of tissue elasticity," Laser Phys. Lett. **10**(7), 075605 (2013).
14. S. Wang, J. Li, R. K. Manapuram, F. M. Menodiado, D. R. Ingram, M. D. Twa, A. J. Lazar, D. C. Lev, R. E. Pollock, and K. V. Larin, "Noncontact measurement of elasticity for the detection of soft-tissue tumors using phase-sensitive optical coherence tomography combined with a focused air-puff system," Opt. Lett. **37**(24), 5184–5186 (2012).
15. C. Dorronsoro, D. Pascual, P. Pérez-Merino, S. Kling, and S. Marcos, "Dynamic OCT measurement of corneal deformation by an air puff in normal and cross-linked corneas," Biomed. Opt. Express **3**(3), 473–487 (2012).
16. D. Huang, E. A. Swanson, C. P. Lin, J. S. Schuman, W. G. Stinson, W. Chang, M. R. Hee, T. Flotte, K. Gregory, C. A. Puliafito, and J. G. Fujimoto, "Optical Coherence Tomography," Science **254**(5035), 1178–1181 (1991).
17. J. Ophir, I. Céspedes, H. Ponnekanti, Y. Yazdi, and X. Li, "Elastography: a quantitative method for imaging the elasticity of biological tissues," Ultrason. Imaging **13**(2), 111–134 (1991).
18. C. L. de Korte, A. F. van der Steen, E. I. Céspedes, and G. Pasterkamp, "Intravascular ultrasound elastography in human arteries: initial experience in vitro," Ultrasound Med. Biol. **24**(3), 401–408 (1998).
19. K. Nightingale, S. McAleavey, and G. Trahey, "Shear-wave generation using acoustic radiation force: in vivo and ex vivo results," Ultrasound Med. Biol. **29**(12), 1715–1723 (2003).
20. R. Muthupillai, D. J. Lomas, P. J. Rossman, J. F. Greenleaf, A. Manduca, and R. L. Ehman, "Magnetic resonance elastography by direct visualization of propagating acoustic strain waves," Science **269**(5232), 1854–1857 (1995).
21. A. Manduca, T. E. Oliphant, M. A. Dresner, J. L. Mahowald, S. A. Kruse, E. Amromin, J. P. Felmlee, J. F. Greenleaf, and R. L. Ehman, "Magnetic resonance elastography: non-invasive mapping of tissue elasticity," Med. Image Anal. **5**(4), 237–254 (2001).
22. M. R. Ford, W. J. Dupps, A. M. Rollins, A. S. Roy, and Z. Hu, "Method for optical coherence elastography of the cornea," J. Biomed. Opt. **16**(1), 016005 (2011).
23. Y. Zhao, Z. Chen, C. Saxer, S. Xiang, J. F. de Boer, and J. S. Nelson, "Phase-resolved optical coherence tomography and optical Doppler tomography for imaging blood flow in human skin with fast scanning speed and high velocity sensitivity," Opt. Lett. **25**(2), 114–116 (2000).
24. S. J. Kirkpatrick, R. K. Wang, and D. D. Duncan, "OCT-based elastography for large and small deformations," Opt. Express **14**(24), 11585–11597 (2006).
25. R. K. Wang, Z. Ma, and S. J. Kirkpatrick, "Tissue Doppler optical coherence elastography for real time strain rate and strain mapping of soft tissue," Appl. Phys. Lett. **89**(14), 144103 (2006).
26. R. K. Wang and A. L. Nuttall, "Phase-sensitive optical coherence tomography imaging of the tissue motion within the organ of Corti at a subnanometer scale: a preliminary study," J. Biomed. Opt. **15**(5), 056005 (2010).
27. M. H. D. Torre-Ibarra, P. D. Ruiz, and J. M. Huntley, "Double-shot depth-resolved displacement field measurement using phase-contrast spectral optical coherence tomography," Opt. Express **14**(21), 9643–9656 (2006).
28. G. Lan, M. Singh, K. V. Larin, and M. D. Twa, "Common-path phase-sensitive optical coherence tomography provides enhanced phase stability and detection sensitivity for dynamic elastography," Biomed. Opt. Express **8**(11), 5253–5266 (2017).
29. J. Li, S. Wang, M. Singh, S. Aglyamov, S. Emelianov, M. Twa, and K. Larin, "Air-pulse OCE for assessment of age-related changes in mouse cornea in vivo," Laser Phys. Lett. **11**(6), 065601 (2014).
30. K. Schwarzschild, *Untersuchungen zur geometrischen Optik: Einleitung in die Fehlertheorie optischer Instrumente auf Grund des Eikonalbegriffs. I* (Druck der Dieterich'schen Univ.-Buchdruckerei (W. Fr. Kaestner), 1905), Vol. 1.
31. R. Kingslake, "WHO? DISCOVERED CODDINGTON'S Equations?" Opt. Photonics News **5**(8), 20–23 (1994).
32. A. E. Conrady, *Applied Optics and Optical Design, Part One* (Courier Corporation, 2013).
33. V. Y. Terebizh, "Two-mirror Schwarzschild aplanats: Basic relations," Astron. Lett. **31**(2), 129–139 (2005).
34. P. Erdös, "Mirror Anastigmat with Two Concentric Spherical Surfaces," J. Opt. Soc. Am. **49**(9), 877–886 (1959).
35. K. Nariai and H. Iwamoto, "A variation of Schwarzschild telescope: golden section solution with two concentric spheres and its extension to finite distance solutions," Opt. Rev. **12**(3), 190–195 (2005).
36. C. Wynne, "Two-mirror anastigmats," JOSA B **59**(5), 572–578 (1969).

Optics EXPRESS

37. A. Gómez-Vieyra, A. Dubra, D. Malacara-Hernández, and D. R. Williams, "First-order design of off-axis reflective ophthalmic adaptive optics systems using afocal telescopes," Opt. Express **17**(21), 18906–18919 (2009).
38. D. Huang, E. A. Swanson, C. P. Lin, J. S. Schuman, W. G. Stinson, W. Chang, M. R. Hee, T. Flotte, K. Gregory, C. A. Puliafito, and et, "Optical coherence tomography," Science **254**(5035), 1178–1181 (1991).
39. M. Born, "E. Wolf Principles of optics," Pergamon Press **6**, 188–189 (1980).
40. D. Malacara-Hernández and Z. Malacara-Hernández, *Handbook of optical design* (CRC Press, 2013).
41. *OpticStudio Help Files* (Zemax LLC).
42. J. W. Ruberti, A. Sinha Roy, and C. J. Roberts, "Corneal biomechanics and biomaterials," Annu. Rev. Biomed. Eng. **13**(1), 269–295 (2011).
43. M. D. Twa, J. Li, S. Vantipalli, M. Singh, S. Aglyamov, S. Emelianov, and K. V. Larin, "Spatial characterization of corneal biomechanical properties with optical coherence elastography after UV cross-linking," Biomed. Opt. Express **5**(5), 1419–1427 (2014).
44. M. Singh, J. Li, Z. Han, S. Vantipalli, C.-H. Liu, C. Wu, R. Raghunathan, S. R. Aglyamov, M. D. Twa, and K. V. Larin, "Evaluating the effects of riboflavin/UV-A and Rose-Bengal/green light cross-linking of the rabbit cornea by noncontact optical coherence elastography," Invest. Ophthalmol. Vis. Sci. **57**(9), 112–120 (2016).
45. S. Vantipalli, J. Li, M. Singh, S. R. Aglyamov, K. V. Larin, and M. D. Twa, "Effects of Thickness on Corneal Biomechanical Properties Using Optical Coherence Elastography," Optom. Vis. Sci. **95**(4), 299–308 (2018).
46. J. Li, Z. Han, M. Singh, M. D. Twa, and K. V. Larin, "Differentiating untreated and cross-linked porcine corneas of the same measured stiffness with optical coherence elastography," J. Biomed. Opt. **19**(11), 110502 (2014).
47. Z. Han, S. R. Aglyamov, J. Li, M. Singh, S. Wang, S. Vantipalli, C. Wu, C. H. Liu, M. D. Twa, and K. V. Larin, "Quantitative assessment of corneal viscoelasticity using optical coherence elastography and a modified Rayleigh-Lamb equation," J. Biomed. Opt. **20**(2), 20501 (2015).
48. M. Singh, J. Li, Z. Han, C. Wu, S. R. Aglyamov, M. D. Twa, and K. V. Larin, "Investigating elastic anisotropy of the porcine cornea as a function of intraocular pressure with optical coherence elastography," J. Refract. Surg. **32**(8), 562–567 (2016).
49. M. Singh, J. Li, S. Vantipalli, S. Wang, Z. Han, A. Nair, S. R. Aglyamov, M. D. Twa, and K. V. Larin, "Noncontact elastic wave imaging optical coherence elastography for evaluating changes in corneal elasticity due to crosslinking," IEEE J. Sel. Top. Quantum Electron. **22**(3), 266–276 (2016).
50. A. Baranne and F. Launay, "Cassegrain: a famous unknown of instrumental astronomy," J. Opt. **28**(4), 158–172 (1997).